

## Automated Recognition of Active Regions on Full Disk Solar Spectroheliograms using $H\alpha$ , Ca II K3 and Fe XII 195 Å wavelengths

Ali Benkhalil, Valentina Zharkova, Stanley Ipson, and Sergei Zharkov  
University of Bradford, BD7 1DP, UNITED KINGDOM

### Abstract

A technique is developed for an automated detection of Active Regions, which are bright areas on a darker background, using  $H\alpha$ , Ca II K3 solar images from the Meudon observatory and EUV (extreme ultraviolet emission) solar images from the EIT (extreme ultraviolet imaging telescope) instrument aboard the Solar and Heliospherical Observatory (SOHO). An initial segmentation of active regions is achieved using intensity thresholds determined from the statistical information obtained from each quarter of full disk solar images. Median filtering and morphological operations are applied to the resulting binary image to remove noise and merge broken regions. The center of gravity of each labeled region is used as a seed for a region-growing procedure. Statistically based local thresholding is applied to calculate upper and lower threshold values defining the spatial extents of the regions. This automated thresholding and region growing (ATRG) procedure has been tested on full-disk solar images from the Meudon observatory for the months April and July 2002 and compared with manually generated synoptic maps. The active regions detected using the ATRG technique were also compared with those of the National Oceanic and Atmospheric Administration observatory (NOAA) giving an average false rejection rate of 1.4 per month and an average false acceptance rate of 0.2 per month. The vertical (pseudo-3D) structures of active regions observed in the corona, chromosphere and the photosphere are presented for the largest feature observed during those months.

**Key Words:** Image processing, segmentation, region growing, solar images, solar features, active regions.

### 1 Introduction

There is a growing number of archives of digitised images of the Sun taken from ground-based and space-based instruments in various wavelengths. These archives are available from different locations and are to be unified by the European Grid of Solar Observations (EGSO) project [2]. The digitised solar images have different sizes, resolutions, instrumental and weather distortions. They all are subject to an automated recognition process in order to provide a reliable location of features and their evolution with time relative to solar rotation. With the growing demand for forecasts of solar activity by the

Space Weather project, the Living with a Star (LWS) project and many industrial organizations, there is a great need for the development of reliable and fast techniques for automated feature recognition on solar disks and their unification into feature catalogues.

The solar atmosphere reveals many features with different characteristics and distinct physical origins. The most clearly distinguished in the  $H\alpha$ -line images are active regions, which are closely associated with sunspots seen in the white light images and plages seen in Ca II K3 spectroheliograms observed from the photosphere. The plages can be large in extent and normally are associated with a strong magnetic field and increased brightness. Bipolar active regions are widely accepted to be the manifestations of emerging buoyant magnetic flux tubes [3, 4, 15] (and the references therein). These flux tubes are seen on the photosphere in white light images as sunspots or in the corona as very diffusive bright areas in extreme ultraviolet (EUV) emission. Filaments on the photosphere or filament channels in the corona are often located alongside active regions separating regions of magnetic fields of opposite polarity [8, 1]. The same active regions are often found to produce numerous flares during their lifetime, in a process that is related to the changes in their magnetic configurations [3, 9]. These magnetic field changes can occur on even smaller scales related to the emergence of mini and nano-flux tubes causing smaller flaring events [9]. This produces different responses at different levels of the solar atmosphere, which allows the testing of theoretical models describing these responses.

Therefore, determining the structure of active regions at various levels of the solar atmosphere can provide a key to the understanding and proper forecast of solar activity manifestations such as: solar flares, coronal mass ejections (CMEs), eruptive filaments, etc. Their reliable automated detection will facilitate the building of a major database of solar active features and enable the analysis of solar activity on a comprehensive database of active regions taken in various wavelengths.

There are three different approaches identified in the literature for the automatic identification of bright active regions (plages). The first is based on the selection of a threshold to separate the object from a background and is straightforward if the intensity histogram is bimodal; otherwise the approach can be difficult [7, 10, 13]. The second approach

is based on region growing techniques segment images into bright and dark regions [5, 12] and is applied in a number of solar images in various wavelengths, including  $H\alpha$ . Finally, the third approach uses the Bayesian inference method for automatically identifying various surface structures on the Sun [11]. All these approaches can give a reasonable accuracy of detection with suitable images, but the Bayesian-based methods are the most computationally expensive. The intensity threshold-based methods are simple and fast, but are relatively sensitive to noise which affects the reliability of the segmentation results obtained.

In order to replace the existing manual detection methods, the current paper presents techniques combining elements of the first two approaches above, threshold and region growing (TRG), for the automated detection of Active Regions (plages) at different heights in the solar atmosphere, which are revealed at different wavelengths. The following types of solar images are used:  $H\alpha$  and Ca II K3 line spectroheliograms from the Meudon observatory and EUV images (Fe XIV 171Å and Fe XII, 195 Å) from SOHO/ Extreme ultraviolet Imaging Telescope (EIT). The work aims at building pseudo-3D reconstructions of detected active regions. The region growing technique, with some modifications, was used in each wavelength in conjunction with intensity thresholds which were applied twice: in the initial processing stage, in order to find seed locations, and in the subsequent active region segmentation. The methods used for active region detection and comparison of the resulting identified regions are discussed in Section 2. Conclusions are given in Section 3.

## 2 The Techniques for Active Regions Recognition

There are two basic assumptions about the solar images made when applying the developed techniques. The first is that the input images are of a standard size ( $1024 \times 1024$  pixel) and the solar disk (radius 420 pixel with centre 511.5, 511.5 pixel) is free of radial limb darkening. In order to comply with this assumption, the techniques are applied to full-disk high-resolution solar images which have been standardized using the procedures for limb fitting, shape correction and limb darkening removal described in reference [14]. At the same time the images are also transformed to the required size. The second assumption is related to one of the properties of active regions, namely, that they are the brightest features on the solar disk. This means that the intensity values inside the detected regions of interest are greater than the intensity values of the local background.

### 2.1 The Initial Segmentation

In order to define a suitable local threshold, all images were first remapped into polar coordinates with origin at the solar disc center. After remapping, statistically-derived localized intensity threshold values were used for an initial segmentation of the bright plages. Pixels whose intensity values are greater than this intensity threshold have their values set to 1 and all other pixels have their values set to zero. The choice of these

initial intensity threshold values is very important because a value that is too high may lead to real features being missed, whereas a value that is too low may lead to noisier binary images and, hence, spurious features. The optimum global threshold value also varies with the image brightness levels and the non-radial large scale intensity variations which are particular problems in some Meudon images. To help overcome these problems, local intensity threshold values ( $T_i$ ) were calculated for top-left, top-right, bottom-left and bottom-right quadrants of each image as follows:

$$T_i = \mu_i + (1 + \Delta_i) \times \sigma_i \quad (1)$$

where  $\mu_i$  is the mean intensity value for the region  $i$ ,  $\sigma_i$  is the standard deviation of the intensity for the same region and  $\Delta_i$  is a constant that was set to 0.3 after investigating more than 30  $H\alpha$ , Ca II K3 and Fe XII 195 Å images. The main stages of this technique are illustrated in Figure 1 for  $H\alpha$ , Figure 2 for Ca II K3, and Figure 3 for Fe XII 195 Å full-disk images, respectively. Subfigures (a) present the cleaned initial images; subfigures (b) show the results of their remapping into the polar coordinates. The results of the initial segmentation based on equation (1) are presented in subfigures (c). Subfigures (d) and (e) show initial and final segmentation results discussed below.

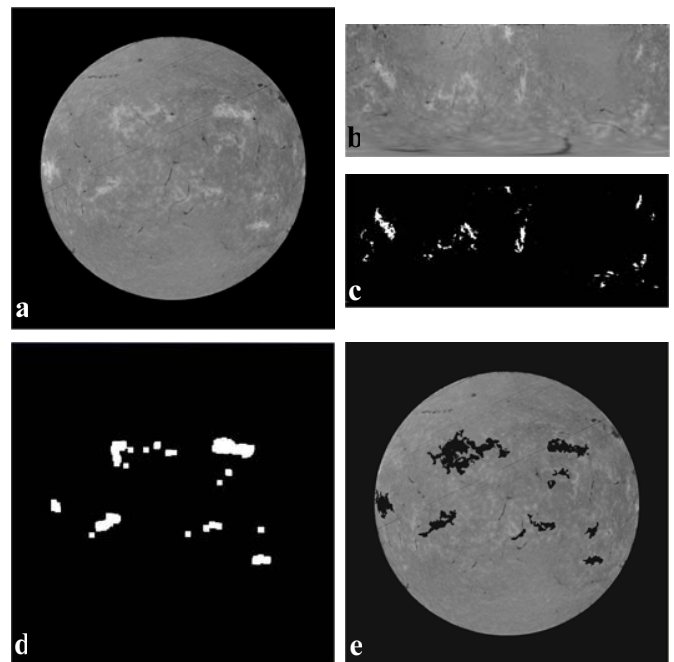


Figure 1: The segmentation procedure stages: a) an original  $H\alpha$  image; b) after a transformation to Polar coordinates; c) after an initial thresholding; d) after a transformation back to the Cartesian coordinates, cleaning and morphological processing; and e) a final result of the region growing

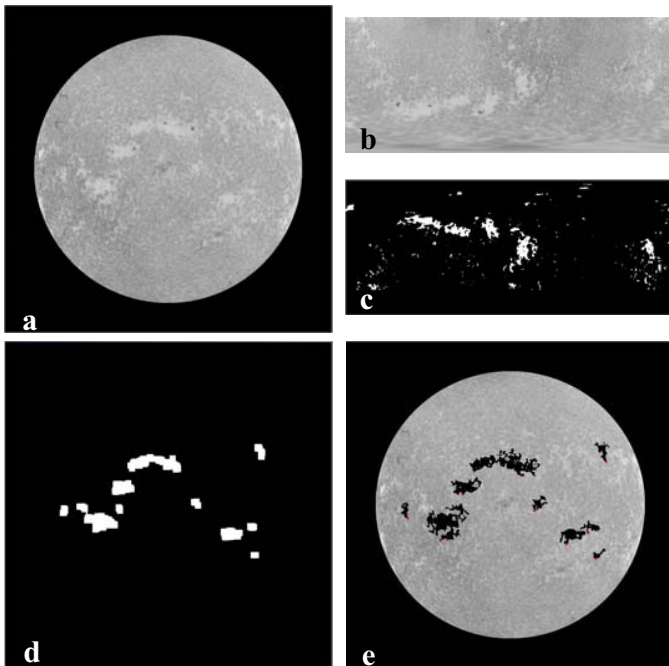


Figure 2: The segmentation procedure stages: a) an original Ca II K3 image; b) after a transformation to Polar coordinates; c) after an initial thresholding; d) after a transformation back to the Cartesian coordinates, cleaning and morphological processing; and e) a final result of the region growing

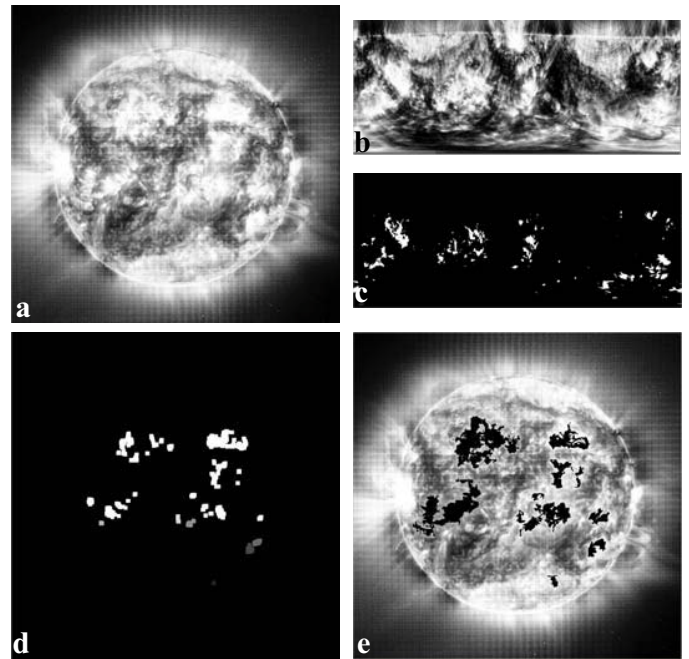


Figure 3: The segmentation procedure stages: a) an original Fe XII 195Å image; b) after a transformation to Polar coordinates; c) after an initial thresholding; d) after a transformation back to the Cartesian coordinates, cleaning and morphological processing; and e) a final result of the region growing

### 2.2 Noise Reduction and Region Labeling

The initial segmentation will generally include noise and unwanted small features caused by over-segmentation. Over-segmentation is preferable to under-segmentation as the former can be remedied using median filtering and morphological operations whereas the latter could lose significant information. First, in order to remove small features a  $7 \times 7$  median filter is used. The size was chosen through experimentation. Morphological opening and closing operations were then applied using a structure element of size  $8 \times 8$ . This smoothed the features and filled in holes. Figures 1(d), 2(d) and 3(d) show the detected regions after applying median and morphological processing and transformation back to Cartesian coordinates. As can be seen, the noise and over-segmentation problems have been significantly reduced.

The result of this initial segmentation is a set of the segments, each of which corresponds to an active region present on the solar disk. Every connected component is numbered, and its centroid is calculated for use as a seed in a region growing procedure. Before using a seed, its location is checked to make sure that it is inside the associated region and, if not, its position is adjusted as follows. A new seed is selected by investigating pixel values in the eight nearest neighbor directions, as illustrated in Figure 4, until a new seed is found inside the region from which the region growing procedure can start.

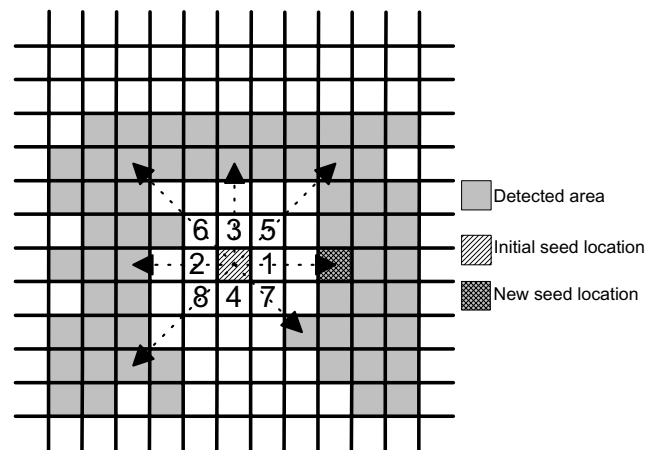


Figure 4: The search scheme for a seed pixel location.

### 2.3 The Region growing technique

The region growing procedure starts with a set of seed pixels and aims to grow a uniform and connected region from each seed. A pixel is added to a growing region if and only if:

- It has not been assigned to another region
- It is an eight-neighbor of the growing region
- The new region created by the addition of a new pixel is still uniform

The region growing algorithm takes as input a standardized image and a corresponding set of seed points obtained by the procedure described in Section 2.2. The algorithm begins at each seed pixel and scans the neighbouring eight pixels in a circular fashion, to determine a membership of the region around the central pixel that complies with the rules above and the following constraints. Two forms of constraint have been considered. The first uses a fixed threshold range (with an upper and lower pixel value), and the second uses a variable threshold range set to a multiple factor of the standard deviation of the pixel values in the current region. After experimentation, the fixed threshold range was chosen as it was found to give more accurate control in defining the outer boundaries of regions while also reducing the occurrence of holes in the regions.

The upper and lower threshold values within initially detected active regions are determined by exploiting the statistical properties of the locally homogeneous background regions. As illustrated in the pseudo code below, the lower threshold value is defined as  $\mu - 0.3\sigma$  (where  $\mu$  is the mean and  $\sigma$  is the standard deviation of that region). This differs from the corresponding threshold used for the initial segmentation. In the case of images in the three wavelengths considered in this paper, the value of the upper threshold was found to be non-critical and was set to the maximum intensity found in each solar disk. As pixels were added, the process repeated with the newly added pixels as the center pixels. For example, when more than one seed pixel has been produced for a single active region, it may happen that two or more regions grow until they touch, in which case they are merged into one contiguous area of active region. During the process, a list of the tested pixels is maintained, in order to avoid unnecessary duplication of the tests. A pseudo-code procedure defining the region growing algorithm is given in Figure 5.

Figures 1(e), 2(e) and 3(e) show the final results of applying the region growing procedure in the H $\alpha$ , Ca K II and Fe XII 195Å images, respectively.

#### 2.4 Image Synchronisation and 3D reconstruction

In order to perform a morphological analysis of the active regions detected in various wavelengths the images have to be synchronized in time, account taken of different view points, matched in size and overlaid. The images in the H $\alpha$  and Ca II K3 wavelengths are obtained from the ground-based observatory in Meudon while the Fe XII, 195Å images are obtained from the SOHO space satellite in the L1 orbital position. These images are in different size and also captured at slightly different time. To synchronize and standardize the images, first the Fe XII, 195Å image that is closest in time to the Meudon H $\alpha$  and CaIIK3 observation is downloaded. The Fe XII, 195Å image is converted to a Map object using the *index2map.pro* IDL function. This object is a structure that contains 2D image data with accompanying pixel coordinate and spatial scale information. The Map object is converted from the SOHO-viewpoint to the Earth viewpoint using the *map2earth.pro* IDL function. To make the dimensions and pixel spacing of the resulting map object identical to the H $\alpha$

```

FOR i=1...n // Run over all n pixels in the image
  REPEAT
    FOR each pixel p at the border of Ri
      FOR all neighbors (x,y) of p
        LOW_THi =  $\mu_i - 0.3 \times \sigma_i$ ; // Let LOW_THi be the
          lowest grey level of pixels in Ri
        HIGH_THi = max(R); // Let HIGH_THi be the
          highest grey level of pixels in R
        IF neighbor unassigned and
          ( $HIGH\_TH_i \geq f(x,y) \geq LOW\_TH_i$ )
          Add neighbor to Ri,
          update HIGH_THi and LOW_THi
      ENDFOR
    ENDFOR
  UNTIL no more pixels are assigned to region
ENDFOR

```

Figure 5: Pseudo-code for the region-growing algorithm where  $R$  is the region of the solar disk,  $R_1, R_2, \dots, R_n$  are a set of regions each starting from an initial seed pixel and  $f(x,y)$  is the grey level of pixel  $x, y$ .

and CaIIK3 images (i.e., size 1024 pixel×1024 pixel, radius 420 pixel and solar centre 511.5 pixel ×511.5 pixel), the *grid\_map.pro* Interactive Data Language (IDL) function is used. Finally, the map objects are converted back to normal index images using the *map2index.pro* IDL function. The images from all three wavelengths are then overlaid and boundaries and pixel values of active regions compared. Figure 6 shows overlaid images from the three wavelengths illustrating the results of the process.

The 3D structure of an active region detected at the three wavelengths: H $\alpha$ , Ca K II and Fe XII 195Å can now be viewed. First the detected regions are cropped from the original images to rectangular fragments of size 380 × 300 pixel. Figure 7 shows the cropped fragments of the same active region detected from images captured on the same day.

Bearing in mind that the images in different wavelengths show features at different heights in the solar atmosphere, it is possible to place these 2D-fragments into a 3-D plot at different heights to indicate their 3D-structure. Figure 8 presents a pseudo-3D structure of these regions showing the effective height of line formation in a given wavelength together with a 3D wire structure of the active region in these wavelengths. A comparison of the active region fragments detected on different heights in solar atmosphere and different times and dates allows us to investigate an active regions morphology, intensity and evolution during its lifetime. This will be the scope of a forthcoming paper.

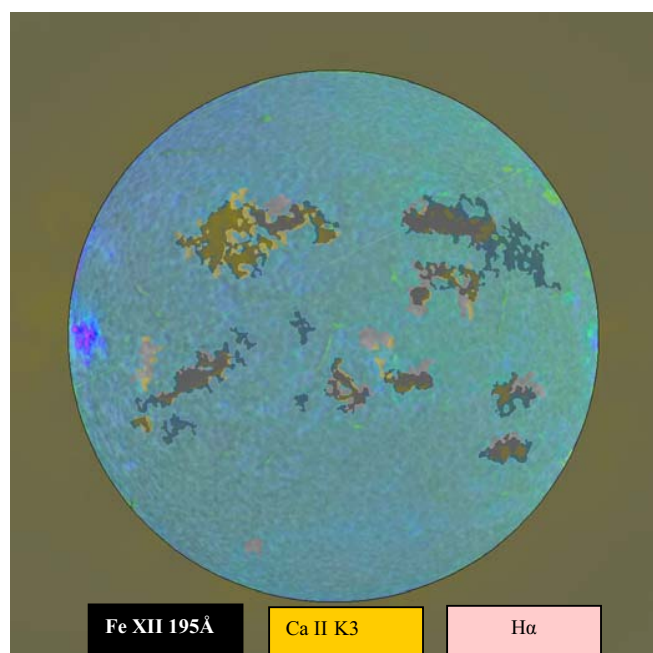


Figure 6: The Active Regions overlaid on the images taken on the same day in the three wavelengths  $H\alpha$ , Ca II K3 and Fe XII 195Å.

## 2.5 The Accuracy of the Technique

The automated threshold and region growing (ATRG) procedure was tested on synoptic image sequences of full-disk solar images from the Meudon observatory for the months of April and July 2002. For further testing the results obtained from the Meudon images were compared with those of the National Oceanic and Atmospheric Administration (NOAA) Observatory and the Big Bear Solar Observatory (BBSO) as illustrated in Table 1 and Figures 9-10.

A quantitative comparison of the results obtained using the ATRG technique, with those done manually at the Meudon observatory [6] and at the BBSO/NOAA observatory is shown in Table 1. In comparison with the other results, those from Meudon detected about 50 percent more active regions on most days. For example, on 11/07/02, there were 19 active regions included in the Meudon results while the ATRG procedure detected only 9 active regions and the NOAA

observatory showed only 8 active regions. In order to quantify these differences, the False Acceptance Rate (FAR) (where we detect an active region and they do not) and the False Rejection Rate (FRR) (where they detect an active region and we do not) were calculated for every day and presented in the last two columns of Table 1. As can be seen, in most cases there is a higher number of active regions detected by the ATRG than by NOAA with an average FAR of 1.8 per day in April and only 1 in July. The FRR was very low at about 0.2 in both April and July, with only five days in each month when we failed to detect a region detected by NOAA. In some cases, as indicated in Figure 9, ATRG detected an active region while NOAA split it into two regions. This affected the quantitative comparison.

We believe the main reason for these differences is due to different definitions of active regions. At Meudon all bright regions (plages) are detected and these are defined as the regions in the chromosphere which are brighter than the normal “quiet” Sun background. At NOAA a detected active region is defined as a bright area on the Sun with a large concentration of magnetic field, often containing sunspots. However, not all plages contain a strong magnetic field as they might be decaying active regions with a weakening magnetic field [3]. Figure 10 clearly illustrates this case by showing the results of active regions detection at NOAA, Meudon and by using the ATRG technique with  $H\alpha$ , Ca II K3 (Meudon) and Fe XII 195Å (SOHO/EIT) solar images on the same day (30/07/02). In Figure 10(e) the Meudon map shows 24 active regions (all the white area (plages) are counted) resulting in double the number detected by the ATRG and NOAA. In general, the agreement with both Meudon and NOAA is good, considering that NOAA bases its decisions at this stage on more information than the ATRG does.

## 3 Conclusions

In this paper an efficient procedure for the automated detection of solar active regions is presented using region growing methods and statistically derived local intensity threshold values. A local intensity threshold is applied to detect bright pixels that are then used as seed candidates for growing active regions. The subsequent region-growing algorithm exploits statistical properties of the locally homogeneous background regions in order to determine the local upper and lower threshold values, which control the

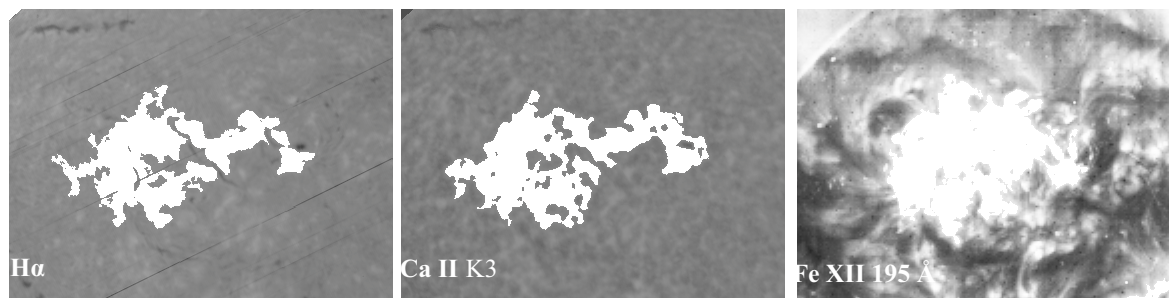


Figure 7: The fragments of the same active region detected from the solar images on 12/04/2002 in the three wavelengths.

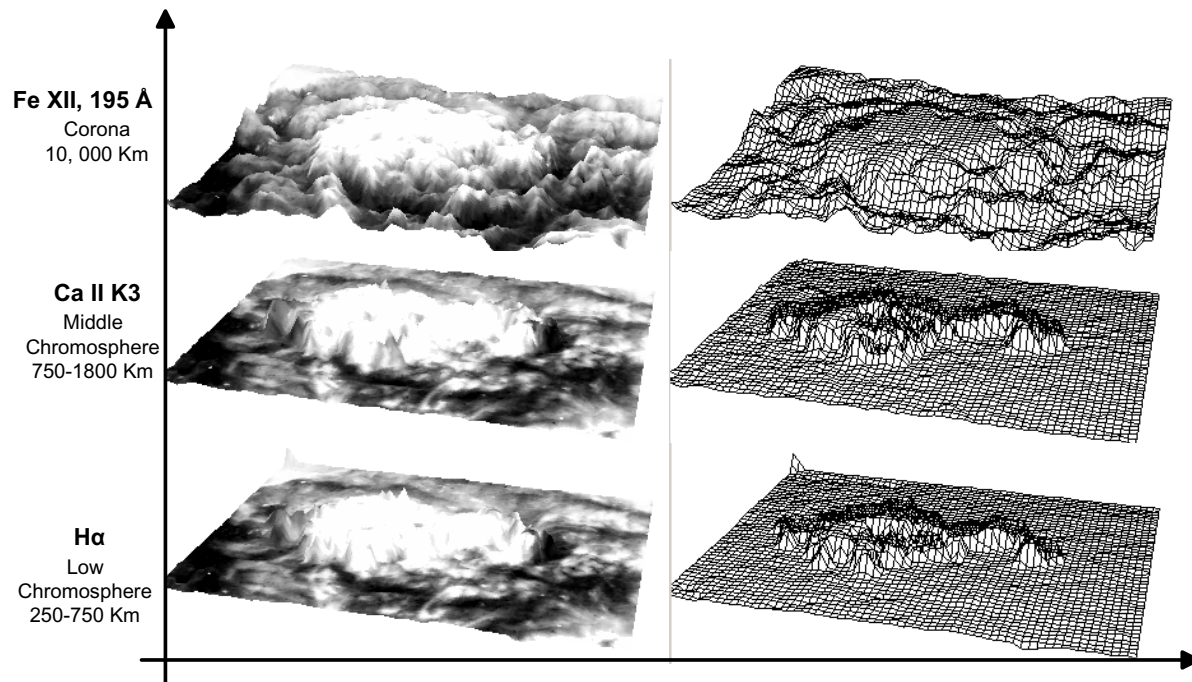


Figure 8: The active region fragments detected from the three wavelengths:  $H\alpha$ , Ca K II, and Fe XII 195Å.

spatial extent of a region growth. The procedures developed have achieved a satisfactory accuracy in the automated detection and segmentation of active regions on the full disk solar images from the Meudon  $H\alpha$ , Ca II K3 and from SOHO/Fe XII 195Å. A pseudo-3D structure for the active regions, detected in these three wavelengths, was estimated to demonstrate the active region variations in different wavelengths which correspond to different heights of the solar atmosphere. A comparison of the active region fragments detected at different heights will allow us to investigate the active region morphology and evolution during its lifetime. This will be the subject of a forthcoming paper.

This research is a part of the European Grid of Solar Observations (EGSO) project funded by the European Commission within the IST Framework 5.

### References

- [1] G. Aulanier and B. Schmieder, "The Magnetic Nature of Wide EUV Filament Channels and Their Role in the Mass Loading of CMEs," *Astronomy and Astrophysics*, 386:1106-1122, 2002.
- [2] R. D. Bentley, "EGSO - The Next Step in Data Analysis," *Proceedings of the Second Solar Cycle and Space Weather Euro-Conference*, 24 - 29 September 2001, Vico Equense, Italy, Edited by Huguette Sawaya-Lacoste, ESA Publication SP-477, 2002.
- [3] L. V; Driel-Gesztelyi, "Emergence and Loss of Magnetic Flux on the Solar Surface," *Proc. SOLMAG the Magnetic Coupling of the Solar Atmosphere : Euroconference and IAU Colloquium 188*, Santorini, Greece, **need vol. number**:113-116, 11-15 June 2002.
- [4] K. L. Harvey, C. Zwaan, "Properties and Emerging of Bipolar Active Regions," *Solar Physics Journal*, 148(1):85-118, 1993.
- [5] M. Hill, V. Castelli, L. Chung-Sheng, C. Yuan-Chi, L. Bergman, J. R. Smith and B. Thompson, "Solarspire: Querying Temporal Solar Imagery by Content," *International Conference on Image Processing*, Thessaloniki, Greece, 1:834-837, 7-10 Oct. 2001.
- [6] Z. Mouradian, "Synoptic Data Findings," *Synoptic Solar Physics ASP Conferences Series*, 140:181-204, 1998.
- [7] D. G. Preminger, S. R. Walton and G. A. Chapman, "Solar Feature Identification using Contrasts and Contiguity," *Solar Physics Journal*, 202(1):53-62, 2001.
- [8] B. Schmieder, O. Engvold, Y. Lin, Y. Y. Deng, N. Mein, "Magnetic Cancellation and Small-Scale Activity in An AR Filament," *Proc. of SOLMAG 2002 the Magnetic Coupling of the Solar Atmosphere: Euroconference and IAU Colloquium 188*, Santorini, Greece, **need vol. number** :223-226, 11-15 June 2002.
- [9] B. Schmieder, G. Aulanier, E. Pariat, M. K. Georgoulis, D. M. Rust and P. N. Bernasconi "Vector Magnetic Field Observations of Flux Tube Emergence," *Proc. of SOLMAG 2002 the Magnetic Coupling of the Solar Atmosphere : Euroconference and IAU Colloquium 188*, Santorini, Greece, **need volume number** :575-580, 11-15 June 2002.
- [10] M. Steinegger, and P. N. Brandt, "On the Determination of the Quiet Sun Centre-to-Limb Variation in Ca K

- Spectroheliograms,” *Solar Physics Journal*, 177(1):287-294, 1998.
- [11] M. Turmon, J. M. Pap, and S. Mukhtar, “Automatically Finding Solar Active Regions Using Soho/Mdi Photograms And Magnetograms,” Proc. SoHO 6/GONG 98 Workshop, Structure and Dynamics of the Interior of the Sun and Sun-like Stars, Boston, 1998.
- [12] A. Veronig, M. Steinegger, W. Otruba, A. Hansmeier, M. Messerotti, and M. Temmer, “Automatic Image Processing In The Frame Of A Solar Flare Alerting System,” *HVAR Observatory Bulletin (HOBUD7)*, 24(1):195-200, 2001.
- [13] J. R. Worden, O. R. White, and T. N. Woods, “Plage and Enhanced Network Indices Derived from CA II K Spectroheliograms,” *Solar Physics Journal*, 177(2):255-264, 1996.
- [14] V. V. Zharkova, S. S. Ipson, S. I. Zharkov, A. K. Benkhalil and J. Abouadarham, “A Full Disk Image Standardisation of the Synoptic Solar Observations at the Meudon Observatory,” *Solar Physics Journal*, 214(1):89-105, 2003.
- [15] C. Zwaan, “Elements and Patterns in the Solar Magnetic Field,” *Ann. Rev. Astron. Astrophys.*, 25:83-111, 1987.

Table 1: A comparison of active regions detected with the ATRG technique with those from Meudon and BBSO/NOAA over April and July 2002 (see explanation in the text).

Date	Meudon		BBSO / NOAA		ATRГ		FAR		FRR		NOTE
	4	7	4	7	4	7	4	7	4	7	
											<b>4 April, 7 July</b>
01	19	15	6	6	8	**	3	**	0	**	We merged 2 regions to 1 (April)
02	14	21	6	6	8	**	2	**	0	**	
03	18	20	9	5	12	7	3	3	0	1	
04	22	20	8	9	11	11	3	1	0	0	
05	**	19	7	9	11	10	6	1	0	0	We merged 2 regions to 1 (April)
06	24	15	9	**	9	**	1	**	0	**	We merged 2 regions to 1 (April)
07	22	19	12	8	13	7	1	0	0	1	
08	24	20	8	8	11	10	4	2	0	0	We merged 2 regions to 1 (April)
09	26	**	11	**	11	**	3	**	0	**	We merged 4 regions to 2 (April)
10	**	20	10	9	15	9	5	0	0	0	
11	**	19	10	8	10	9	2	1	0	0	We merged 4 regions to 2 (April)
12	20	18	11	6	8	7	0	1	0	0	We merged 6 regions to 2 (April)
13	21	16	12	5	**	5	**	0	**	**	
14	21	17	9	6	10	8	1	2	0	0	
15	22	16	6	**	7	**	1	**	0	**	
16	20	18	7	9	7	10	0	1	0	0	
17	19	19	6	7	6	7	0	0	0	0	
18	18	17	5	6	7	7	2	2	0	1	
19	21	18	6	4	7	4	1	0	0	0	
20	17	19	6	4	6	4	0	0	0	0	
21	15	19	7	4	9	6	2	2	0	0	
22	14	16	7	5	8	7	1	2	0	0	
23	15	22	9	9	9	10	3	1	2	0	We merged 2 regions to 1 (April)
24	17	22	8	**	9	**	3	**	2	**	
25	14	22	10	12	10	13	0	1	0	0	
26	11	24	8	12	**	12	**	0	**	**	
27	11	23	6	12	8	13	3	1	1	0	
28	7	24	8	13	7	13	0	1	1	1	
29	6	22	7	12	7	12	2	0	1	0	We merged 2 regions to 1 (April) & (July)
30	**	24	7	12	8	12	1	1		0	We merged 3 regions to 1 (July)
31	**	24	**	10	**	9	**	2	**	1	
Total	<b>458</b>	<b>588</b>	<b>241</b>	<b>216</b>	<b>251</b>	<b>222</b>	<b>53</b>	<b>25</b>	<b>7</b>	<b>5</b>	<b>**no data on that day</b>

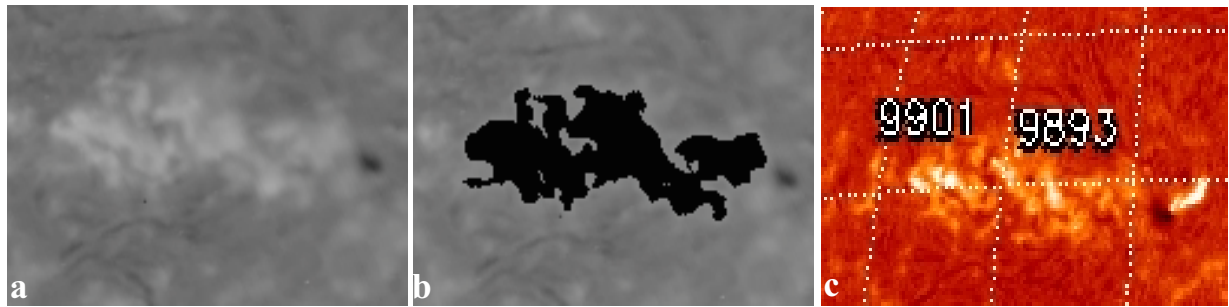


Figure 9: An example of two active regions merging: a) the Meudon  $H\alpha$  input image, b) the same image after applying the region growing procedure, and c) the BBSO  $H\alpha$  image showing the same region is divided into two active regions.

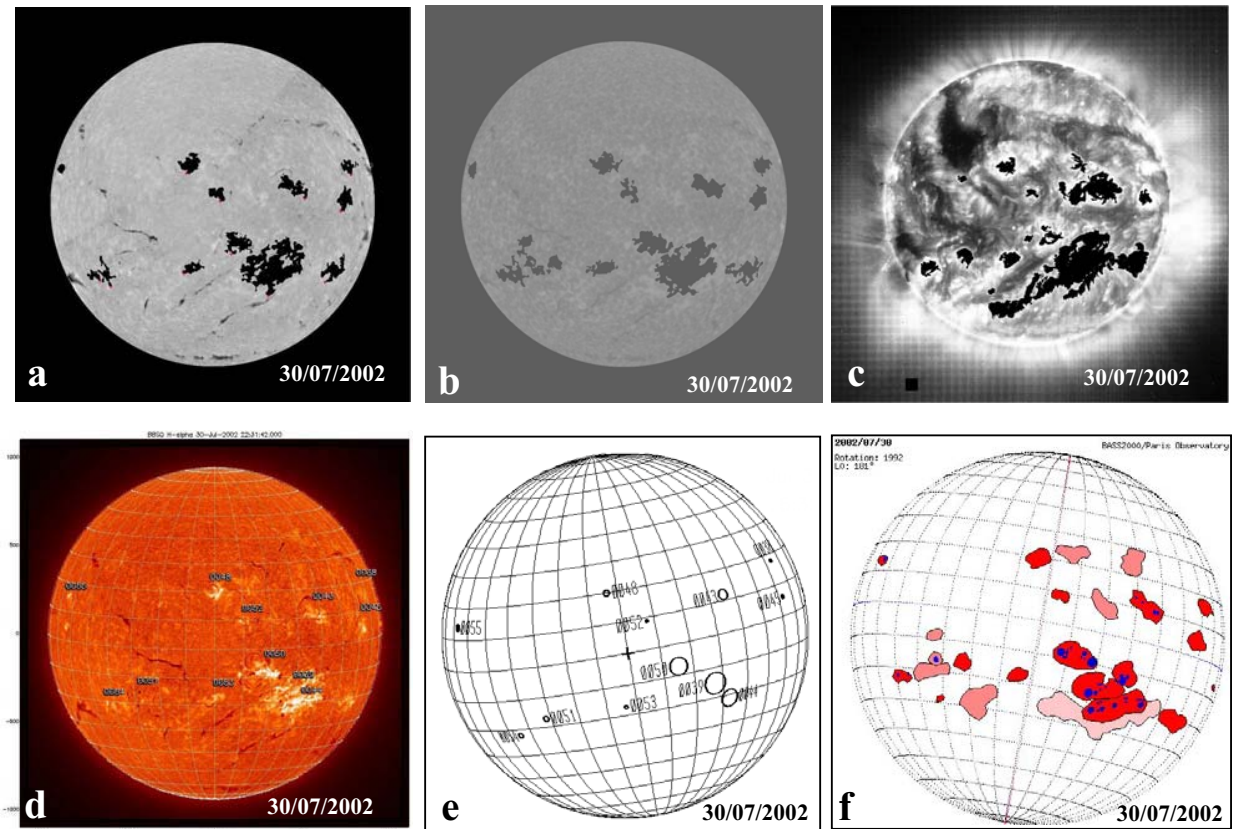


Figure 10: A comparison of active region detection results: (a) ATRG procedure applied to  $H\alpha$ ; (b) ATRG procedure applied to  $Ca\ II\ K3$ ; (c) ATRG procedure applied to  $Fe\ XII\ 195\text{\AA}$ ; (d) BBSO solar image showing 12 active regions; (e) BBSO solar map showing 12 active regions; (f) Meudon solar map showing 24 active regions.